

Experimental investigation on debonding behavior of Fe-SMA-to-steel joints

Lingzhen Li^{a,b,*}, Wandong Wang^c, Eleni Chatzi^b, Elyas Ghafoori^{a,b,*}

^a Empa, Swiss Federal Laboratories for Materials Science and Technology, Überlandstrasse 129, 8600, Dübendorf, Switzerland

^b Institute of Structural Engineering (IBK), Department of Civil, Environmental and Geomatic Engineering (D-BAUG), ETH Zürich, 8093, Zürich, Switzerland

^c School of Civil Aviation, Northwestern Polytechnical University, Xi'an, Shaanxi 710072, China

ARTICLE INFO

Keywords:

Iron-based shape memory alloy (Fe-SMA)

Bond-slip behavior

Bond capacity

Debonding propagation

Steel strengthening

ABSTRACT

This work is the first systematic study on the static behavior of adhesively-bonded Fe-SMA-to-steel joints in applications adopting iron-based Shape Memory Alloys (SMAs). In order to provide a better understanding on the mechanical behavior of the adhesively bonded joint, an experimental campaign was established, involving 24 lap-shear tests in a displacement-controlled loading regime. The test series includes two types of Fe-SMAs (non-prestrained and prestrained), three types of adhesives (SikaDur 30, Araldite 2015, and SikaPower 1277), and three different thickness values (0.5, 1, and 2 mm) for the adhesive. A digital image correlation (DIC) technique was employed to measure the full-field displacement and strain, which were then used to infer the shear behavior. The mechanical behavior was analyzed on the basis of the experimentally derived load-displacement curves, the shear stress profiles along the bond line, and the bond-slip curves; three stages were observed during the loading process of a bonded joint: (i) a linear stage, (ii) a damage accumulation stage, and (iii) a debonding propagation stage. The test results indicate that a more ductile adhesive or a thicker adhesive layer possess a higher fracture energy, leading to a greater bond capacity. The results were also compared against those from lap-shear tests on carbon fiber reinforced polymer (CFRP) bonded joints. It is found that an Fe-SMA bond and a CFRP bond behave similarly when a linear adhesive is utilized; a nonlinear adhesive, however, results in significant mechanical differences between the two bonded joints, which merit individual analysis.

1. Introduction

The repair and strengthening of aging structures can increase their lifetime, while lowering the impact on greenhouse gas (GHG) emissions that stems from replacement. The development of new repair and strengthening systems, which adopt advanced materials, brings potential for bolstering the sustainability index of civil infrastructures [1]. Aging infrastructures worldwide, a large portion of which comprise steel bridges, are suffering from degrading mechanical performance [2, 3]. A major source of this problem, limiting the service life of steel infrastructures, is the accumulation of fatigue damage due to cyclic loading [4,5]. The strengthening and repair of these aging steel structures offer a twofold benefit to worldwide economies and societies. The first benefit pertains to cost savings from alleviation of decommissioning and replacement of existing structures. The second relates to no (or minimal) interruption of the operation of these infrastructures.

1.1. Existing strengthening methods

There are several existing methods to combat the fatigue problems and improve the mechanical performance of steel structures. The principal mechanism of fatigue strengthening is to reduce the stress level at the fatigue-prone details typically via (i) enhancing the local stiffness and (ii) introducing local compression. Examples of the former case are paving a layer of ultra-high performance concrete (UHPC) on the orthotropic steel decks (enhancing the local bending stiffness) [6,7] and bonding carbon fiber reinforced polymer (CFRP, improving the local tensile stiffness) [8,9] to the fatigue sensitive locations. The high frequency mechanical impact (HFMI) at the welding details [10,11] belongs to the latter case, introducing local compression. To enjoy the benefits of both the enhanced stiffness and the introduced compression, the unbonded [12,13] and bonded [14] prestressed CFRP strengthening scheme, which requires mechanical clamps and hydraulic jacks, has been developed. Infinite fatigue life can be realized, if sufficient pre-stress level is introduced. The prestressed strengthening solutions using

* Corresponding author at: Empa, Swiss Federal Laboratories for Materials Science and Technology, Überlandstrasse 129, 8600, Dübendorf, Switzerland.

E-mail addresses: lingzhen.li@empa.ch (L. Li), w.wang@nwpu.edu.cn (W. Wang), chatzi@ibk.baug.ethz.ch (E. Chatzi), elyas.ghafoori@empa.ch (E. Ghafoori).

<https://doi.org/10.1016/j.conbuildmat.2022.129857>

Received 19 July 2022; Received in revised form 26 October 2022; Accepted 21 November 2022

0950-0618/© 2022 The Author(s). Published by Elsevier Ltd. This is an open access article under the CC BY license (<http://creativecommons.org/licenses/by/4.0/>).

CFRP have substantiated highly efficient schemes for rehabilitation of steel structures.

However, when the use of mechanical clamps and hydraulic jacks is restricted (e.g., drilling holes in the steel substrate for the mechanical clamps is undesired), the prestressed CFRP solution is hardened. As a remedy, a bonded strengthening solution based on Nickel–Titanium (NiTi)-SMA wires embedded in CFRP composites has been developed [15–17]. The prestress, which is transferred to the parent structure via the adhesive bond, can be easily effectuated by heating the prestrained NiTi-SMA, followed by a cooling process. Since the E-modulus of the NiTi-SMA is rather low (14–90 GPa) [15,16,18,19], its contribution to the additional stiffness can be ignored. As a result, the stiffness and compression are attributed to the CFRP composites and NiTi-SMA wires, respectively. So far, two major limitations of such a NiTi-SMA-CFRP composites strengthening solution are the price of the NiTi-SMA materials and the time-consuming fabrication of the composite patches. Hence, a more suitable SMA solution is desired for the engineering application.

1.2. Bonded Fe-SMA strengthening solution

The iron-based SMA (Fe-SMA) developed at Empa (Swiss Federal Laboratories for Materials Science and Technology) is an ideal alternative, as (i) its price is substantially lower than that of NiTi-SMA (and only a few times that of the mild steel) and (ii) its E-modulus in the quasi-linear stage (160–180 GPa) [20–22] is comparable to that of the normal-modulus CFRP. The comparable stiffness of Fe-SMA strips and CFRP composites leads to the next benefit, i.e., (iii) alleviation of the need to assemble the Fe-SMA-CFRP composite patches, which results in time savings. Thus far, the mechanically clamped Fe-SMA strips have been successfully employed in fatigue strengthening of steel plates [23] and steel girders [24,25].

As the use of mechanical clamps is occasionally restricted, the bonded strengthening of steel structures using Fe-SMA offers further potential, as it possesses the following benefits: (i) getting rid of complex equipment, such as heavy hydraulic jacks and mechanical fixation, (ii) inducing no damage to the parent structure via drilling holes for mechanical clamps, and (iii) allowing for gradual stress transfer along the bond length. Thus far, only very limited studies [26,27] have been conducted for investigating the behavior of such an SMA-based retrofitting solution.

An Fe-SMA strip can be bonded onto the target position of the steel structure, which is to be strengthened, via use of an adhesive, as demonstrated in Fig. 1. After the adhesive is cured, the mid-portion of the Fe-SMA strip is heated to a target temperature by flame [15] or electricity [28], followed by cooling to the room temperature; prestress is generated in this middle region due to a martensite to austenite phase transformation of the Fe-SMA [29]. This process is known as the activation of prestress. Note, only the middle portion is activated to mitigate the chance of debonding failure over the anchorage area, due to the elevated temperature. The reason is that the elevated temperature degrades the mechanical performance of the adhesive, especially when the temperature is close to or exceeds the glass transition temperature [30,31], resulting in a significantly reduced stress transferring capacity (bond capacity) [30–32]. Therefore, the two ends of the Fe-SMA strip remain unheated and are designed as the bonded anchorage zone, which transfers the generated prestress to the parent structure. For this reason, the bonded anchorage zone is a critical component of the strengthening system, which renders the understanding of its mechanical behavior a crucial aspect. To the knowledge of the authors, the only published study investigating the bond behavior between Fe-SMA and steel has been delivered by Wang et al. [27], where a lap-shear model was employed to simulate the bonded anchorage zone, as illustrated in Fig. 2. A more systematic investigation on the mechanical behavior of Fe-SMA bonded joints is needed to gain insights into the structural integrity of such a bonded prestressed strengthening solution.

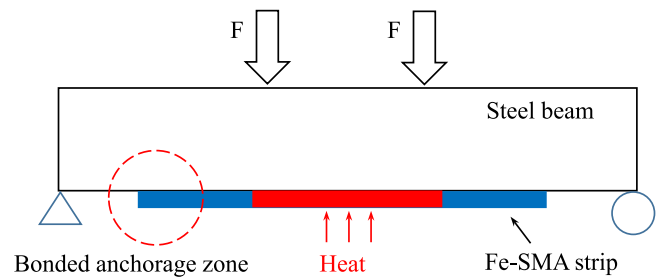


Fig. 1. Schematic view of a steel beam strengthened by bonded Fe-SMA strip.

The current work is the first systematic study on the static mechanical behavior of adhesively bonded Fe-SMA-to-steel joints. 24 Fe-SMA-to-steel lap-shear specimens were tested under quasi-static monotonic loading with displacement control. The effect of loading speed, adherent type, adhesive type, and adhesive thickness were taken into consideration. A digital image correlation (DIC) technique was used to measure the full-field displacement and strain profiles of the surface of the Fe-SMA and steel elements. The measured displacement and strain were then post-processed to infer the shear behavior in the adhesive bond. The failure mode, bond capacity, and load–displacement behavior were analyzed. The test results validate the potential delivered by the bonded Fe-SMA solution for strengthening of steel structures.

2. Experimental procedures

2.1. Materials and dimensions

Every single lap-shear specimen employed in this study, as shown in Fig. 2, consists of three materials: (i) a steel plate as the substrate material, (ii) an Fe-SMA strip bonded on top and pulled toward one direction, and (iii) an adhesive used to bond Fe-SMA onto the steel plate. Their geometry is described below with the corresponding mechanical properties presented in Table 1.

2.1.1. Fe-SMA

Non-prestrained and prestrained Fe-SMA strips are used in this study to investigate the influence of adherent type. The prestrained Fe-SMA strip is formed by a non-prestrained Fe-SMA strip tensioned to 2% strain, followed by an unloading process to a zero force, with ca. 1.3% permanent residual strain, which is constituted by phase transformation strain and plastic strain [33]. All strips are 1.5 mm in thickness and 50 mm in width. The mechanical properties of the two Fe-SMAs are tested in form of dog-bones (Fig. 3(a)) following Mohri et al. [34]. Existing studies [35,36] indicate that the Fe-SMA suffers from significant creep and relaxation phenomena, which implies a loading-rate dependency. In view of this, the dog-bone tests were conducted under displacement control with a strain rate of 1×10^{-4} /s, which is equivalent to the rate adopted in the lap-shear tests. The stress–strain behaviors of non-prestrained and prestrained Fe-SMA are plotted in red and blue in Fig. 4, respectively. During the lap-shear tests, the debonding length increased while the loading speed was kept constant. Thus, the strain rate of the Fe-SMA strips correspondingly decreased. In order to reveal the potential impact of this phenomenon on the results, the non-prestrained Fe-SMA dog-bones were tensioned with a reduced strain rate of 5×10^{-5} /s, corresponding to the strain rate of Fe-SMA strip short before full debonding. The stress–strain behavior at reduced strain rate is presented in green in Fig. 4, which yields almost indistinguishable behavior when compared against the regular strain rate. Therefore, the stress–strain behaviors measured with a strain rate of 1×10^{-4} /s were exploited to represent that in the lap-shear tests.

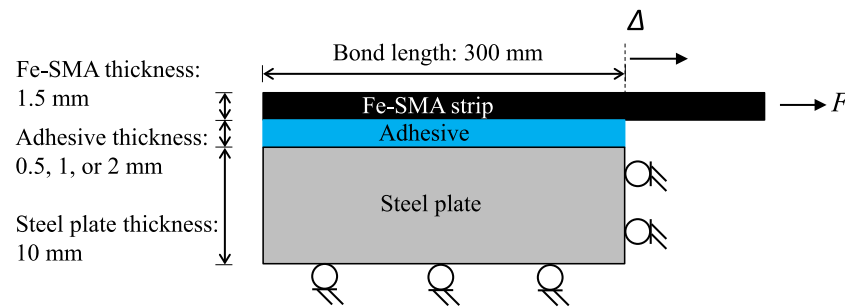


Fig. 2. Schematics of the lap-shear model, simulating the bonded anchorage zone (bond width of 50 mm not shown). Δ with a dashed line is referred to as the loaded end.



Fig. 3. Dog-bone samples: (a) steel or Fe-SMA, (b) SikaDur 30, (c) Araldite 1515, and (d) SikaPower 1277. The relative size in the picture roughly reflects the size in reality.

2.1.2. Adhesives

To investigate the impact of ductility of adhesives, three types of two component epoxy adhesives were utilized for bonding. To attain the mechanical properties of each adhesive, the adhesive dog-bone samples were prepared with an overall length of 185 mm and a cross-section at the narrow part of 10×3 mm, and tested according to ISO 527-2:2012 [37] with a strain rate of 1%/min. Interested readers are referred to Michels et al. [38] for details of sample dimensions and the further testing procedure. The measured stress–strain behavior of the three adhesives is plotted in Fig. 5. SikaDur 30 (in black, referred to as Sika 30 hereinafter), is a linear adhesive, with stress–strain behavior almost following a straight line; Araldite 2015 (in blue) and SikaPower 1277 (in red, referred to as Sika 1277 hereinafter) are nonlinear adhesives, as their stress–strain behavior experience an obvious plateau. To investigate the influence of the adhesive thickness, the bond line was prepared with three different target thicknesses of 0.5, 1, and 2 mm and a constant length of 300 mm.

2.1.3. Steel

The steel plate is 500 mm in length, 250 mm in width, and 10 mm in thickness. The E-modulus, 200 GPa, was measured in the form of dog-bones with the same geometry and loading speed of Fe-SMA.

2.2. Specimen preparation

To enhance the bond performance between Fe-SMA strips and steel plates, the target bonding areas were sand-blasted to remove the oxidized layer and increase the roughness [39,40]. Prior to and after

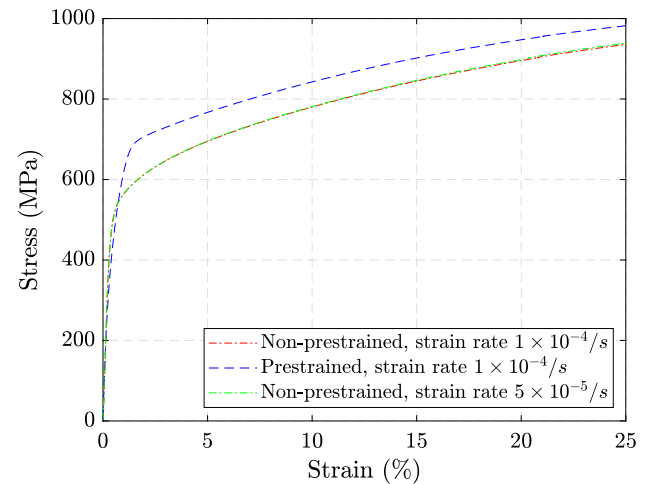


Fig. 4. Stress–strain curves of Fe-SMA. Non-prestrained at regular strain rate in red; prestrained at regular strain rate in blue; non-prestrained at reduced strain rate in green. (For interpretation of the references to color in this figure legend, the reader is referred to the web version of this article.)

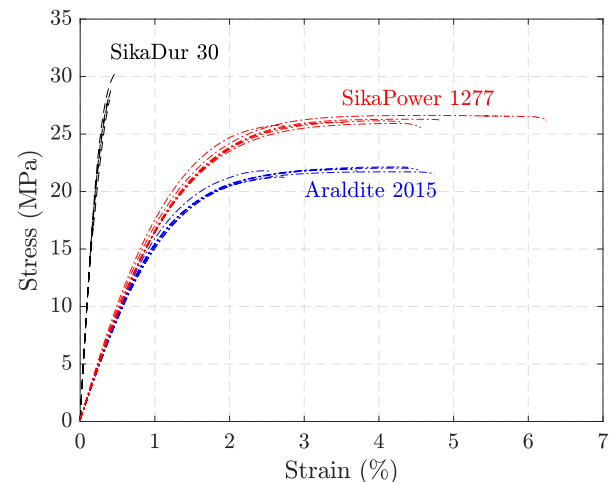


Fig. 5. Stress–strain behaviors of adhesives, with Sika 30 in black, Araldite 2015 in blue, and Sika 1277 in red. (For interpretation of the references to color in this figure legend, the reader is referred to the web version of this article.)

sand-blasting, the bonding areas were washed by acetone-dipped cotton cloths to remove grease and dusts. The pressed air was then used to blow away the residual of cotton fibers from the cleaning cloths.

After the surface preparation, the two components of the adhesive were mixed following the manufacturer guidelines and then applied on the bonding areas of Fe-SMA strips and steel plates. Next, the Fe-SMA

Table 1
Material properties.

Material	E-modulus (MPa) (CoV in %) ^a	Tensile strength (MPa) (CoV in %) ^a	Elongation at break (%) (CoV in %) ^a
Steel	200,320 (9.6)	453 (0.3)	23
Non-prestrained Fe-SMA	153,300 ^b (5.6)	1023	53
Prestrained Fe-SMA	137,500 ^b (7.7)	1022	50
SikaDur 30	10,327 (2.69)	28.94 (3.62)	0.42 (11.08)
Araldite 2015	1,870 (1.91)	21.82 (1.45)	3.77 (25.01)
SikaPower 1277	1,952 (3.59)	26.13 (1.15)	4.37 (27.28)

^aCoV designates the coefficient of variation, which is provided in parentheses if relevant statistics is available.

^bChord modulus between stress of 20 MPa and 300 MPa. 300 MPa is empirically chosen, as the initial quasi-linear stage of Fe-SMA is observed to reach a nominal yield stress of 300–350 MPa.

strips were positioned onto the steel plates and subjected to pressure under heavy weight to remove excessive adhesive. A straight artificial debonding tip was formed by a thin teflon tape placed on the steel plate at the loaded end, which is situated 300 mm away from the free end; it ensures (i) a bond length of 300 mm, which is identical to the design, and (ii) an identical geometry of debonding tip in all specimens. Spacers were placed in between the Fe-SMA strip and the steel plate to control the adhesive thickness. The prepared specimens were cured in a climate room under a stable temperature of 20 °C and a relative humidity of 50% for at least two weeks. Details of all 24 joints are listed in Table 2. The first segment in the specimen symbol represents the adherent type, with “NS” and “PS” denoting non-prestrained and prestrained Fe-SMA strips, respectively; the second segment indicates the adhesive type, with “S1”, “A”, and “S2” denoting Sika 30, Araldite 2015, and Sika 1277, respectively; in the third segment, the digit after “T” means the target adhesive thickness (in mm); to explore the repeatability of lap-shear joints, two nominally identical specimens were tested, denoted by “1” and “2” in the fourth segment.

Before the lap-shear tests, a black speckled pattern on white background was painted onto the surface of the specimens to facilitate the subsequent measurement of the full-field displacement and strain by means of the DIC technique. The main reason for employing a DIC measurement system in place of a more traditional technique, such as strain gauges, resides in three advantages of the DIC technique, which meet the requirement of the current study. The first pertains to the ability of measuring large strains (larger than 10% in our case), while typical strain gauges only measure up to 3%–5%. The second benefit lies in the high spatial resolution, which allows for capturing the peak shear stress [27] with sufficient precision and gathering more data for statistical analysis (Section 5.4). The third advantage is the potential for full-field displacement and strain measurements, which enables analysis across the entirety of the whole measurement field of interest (Section 5.7). A brief introduction of the DIC strain measurement can be found in Appendix.

2.3. Lap-shear tests

Lap-shear tests were then conducted under displacement control using the setup shown in Fig. 6. Employing a displacement-control protocol is important for ensuring stable fracture in the bonded joint. The steel plate of the specimen was fixed onto a thick steel base by means of two thick steel bars. The extension of the Fe-SMA strip was held in place by a mechanical clamp and pulled by a hydraulic jack. A load cell with a capacity of 150 kN was used to measure the tensile force, while a LVDT was used to measure the displacement of the hydraulic cylinder, whose loading speed was controlled at 0.02 mm/s. All specimens were tested until failure, namely full debonding or rupture of the Fe-SMA strip.

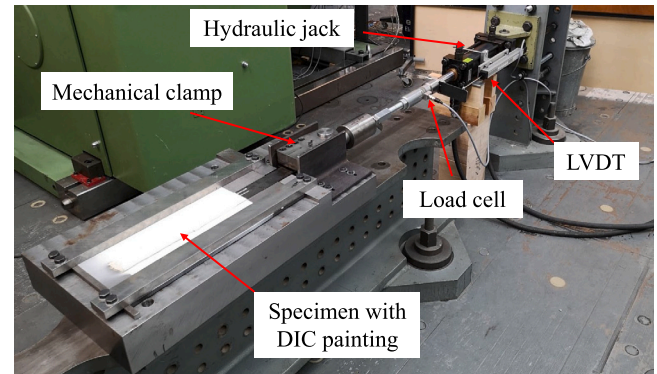


Fig. 6. Lap-shear test setup.

3. Post-processing

3.1. Tensile strain of Fe-SMA strips

The DIC strain reading indicates that the Fe-SMA tensile strain along the width direction corresponds to a curved profile, see Fig. 7. As 2D behavior is non-trivial to process, we here resort to a two-point Gauss integral approximation, per Eq. (1), which is used to approximate an average strain along the strip width direction, thus degenerating the analysis to a 1D problem.

$$\epsilon_{mean} = \frac{\epsilon_{-1/\sqrt{3}} + \epsilon_{1/\sqrt{3}}}{2} \quad (1)$$

where $\epsilon_{-1/\sqrt{3}}$ and $\epsilon_{1/\sqrt{3}}$ are the tensile strain of the Fe-SMA strip at Gauss points of $\pm w/2\sqrt{3}$, with w denoting the width of the Fe-SMA strip. Besides, the three-point integral is also explored, which yields a similar strain approximation to the two-point integral. However, not all three integral points of all 24 specimens can be consistently covered by the DIC strain reading. Thus, a two-point rather than a three-point Gauss integral is eventually employed.

3.2. Tensile stress of Fe-SMA strips

Substituting the tensile strain computed via Eq. (1) into the constitutive relationship of the Fe-SMA material (stress–strain relationship, as shown in Fig. 4), yields the tensile stress behavior.

3.3. Force–displacement of bonded joints

The force–displacement behavior of bonded joints can be derived via the tensile stress behavior of Fe-SMA strips inferred from the previous step. In this study, two sets of load–displacement curves are processed for each specimen. In the first curve, the load is directly measured by the load cell; this is regarded as a precise (reference)

Table 2
Test matrix.

Specimen No.	Specimen symbol	Adherend	Adhesive	Adhesive thickness (mm)	Bond capacity (kN)	Effective bond length (mm)	Failure mode ^a
1	NS-S1-T0.5-1	Non-prestrained Fe-SMA	SikaDur 30	0.5	38.87	68	C
2	NS-S1-T0.5-2				38.98	64	C
3	NS-A-T0.5-1		Araldite 2015		55.87	135	C+A
4	NS-A-T0.5-2				56.21	133	C+A
5	NS-S2-T0.5-1		SikaPower 1277		59.09	121	C
6	NS-S2-T0.5-2				58.93	125	C
7	PS-S1-T0.5-1	Prestrained Fe-SMA	SikaDur 30	0.5	33.55	68	C
8	PS-S1-T0.5-2				35.37	74	C
9	PS-S1-T1-1			1	34.66	73	C
10	PS-S1-T1-2				35.54	83	C
11	PS-S1-T2-1			2	36.69	81	C
12	PS-S1-T2-2				37.95	82	C
13	PS-A-T0.5-1	Prestrained Fe-SMA	Araldite 2015	0.5	59.99	134	C+A
14	PS-A-T0.5-2				59.54	132	C+A+R
15	PS-A-T1-1			1	62.13	145	C+A
16	PS-A-T1-2				60.55	142	C+A+R
17	PS-A-T2-1			2	60.32	144	C+A+R
18	PS-A-T2-2				63.05	169	C+A
19	PS-S2-T0.5-1	Prestrained Fe-SMA	SikaPower 1277	0.5	61.77	137	C
20	PS-S2-T0.5-2				62.33	139	C+R
21	PS-S2-T1-1			1	64.49	143	C
22	PS-S2-T1-2				65.27	145	C
23	PS-S2-T2-1			2	63.14	N/A ^b	C+R
24	PS-S2-T2-2				66.79	162	C

^aC: cohesion failure; A: adhesion failure; R: Fe-SMA strip rupture.

^bThe shear stress profile was not fully developed due to an early rupture of the Fe-SMA strip.

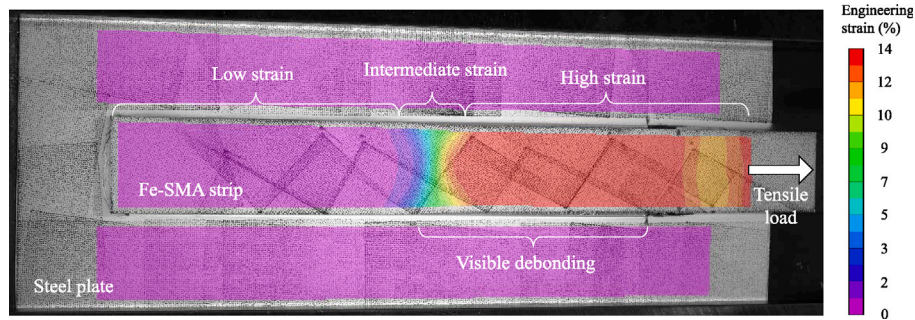


Fig. 7. A typical strain contour of the Fe-SMA strip (specimen PS-S2-T2-2 as an example), with purple color, green color, and red color reflecting low, intermediate, and high strain levels, respectively. Debonding is visible in the region corresponding to the intermediate and high strain zones. (For interpretation of the references to color in this figure legend, the reader is referred to the web version of this article.)

value. In the second curve, the load is estimated through multiplication of the tensile stress at the loaded end with the cross-sectional area. The displacement measured by the LVDT inherently contains the elongation of the connection bars between the mechanical clamp and the hydraulic jack and cannot be directly exploited. We, thus, resort to the displacement read by the DIC at the loaded end (Fig. 2) to represent the displacement of the bonded joint.

3.4. Shear behavior

A simple relationship, as described in Fig. 8 and Eq. (2), which considers the equilibrium in the longitudinal direction, is used to infer the shear stress at the bonded side of Fe-SMA strips, which is the same as the shear stress of the adhesive layer.

$$\tau = t \cdot \frac{d\sigma}{dx} \quad (2)$$

where τ and σ are the shear and tensile stress of the Fe-SMA strip; t represents the thickness of Fe-SMA strips; x is the coordinate in the longitudinal direction.

The shear stress ($\tau(x)$) is processed using Eq. (2), while the slip ($s(x)$), which is the relative displacement between the Fe-SMA strip and

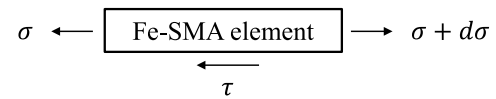


Fig. 8. Equilibrium of an infinitesimal element of the Fe-SMA strip. σ and τ represent the tensile and shear stress, respectively.

the steel plate, is measured by the DIC technique. Correlating the shear stress ($\tau(x)$) and the slip ($s(x)$) by the coordinate (x), the shear-slip ($\tau(s)$) relationship, namely bond-slip relationship, is obtained.

4. Results and discussion

4.1. Failure mode

In the design of an adhesively bonded joint, cohesion failure, where damage initiates and propagates inside the adhesive layer, is preferred; in this case, the mechanical behavior of the bonded joint is mainly controlled by the adhesive, rather than the adhesive-adherent interface [41,42]. An adhesion failure, i.e., failure in the adhesive-adherent

interface, is not favored, since the surface quality, which can hardly be quantified, plays an important role. Among all 24 tested lap-shear joints, specimens with Sika 30 and Sika 1277 adhesives failed under cohesion type (see Figs. 9(a) and 9(c)), and specimens with Araldite 2015 adhesive failed under major cohesion and minor adhesion (see Fig. 9(b)). Despite the minor adhesion failure, their bond capacities were so high that three out of six joints with prestrained Fe-SMA bonded with Araldite 2015 had Fe-SMA rupture. Thus, the surface preparation and the associated failure mode are not further investigated in this study.

Such an Fe-SMA rupture also occurred for two specimens with prestrained Fe-SMA bonded by Sika 1277 adhesive. It should be noted that the nominal tensile stress and strain in the Fe-SMA strips at rupture are 794–842 MPa and 6.1–10 %, respectively, which are significantly lower than those in the unidirectional tensile tests (1022 MPa and 50%). The reasons are yet clear; they might be attributed to an eccentric loading and a local strain concentration of the Fe-SMA strip. More investigation on the premature rupture of the Fe-SMA is needed. However, the fracture surface in the bond line of these five specimens with Fe-SMA rupture will assist the explanation the bond-slip behavior in Section 5.6.

4.2. Full-range behavior

This section describes the full-range mechanical behavior of a bonded joint over three stages: the elastic stage, the damage accumulation stage, and the debonding propagation stage. Specimen PS-S2-T0.5-2 is used as an example.

4.2.1. Elastic stage

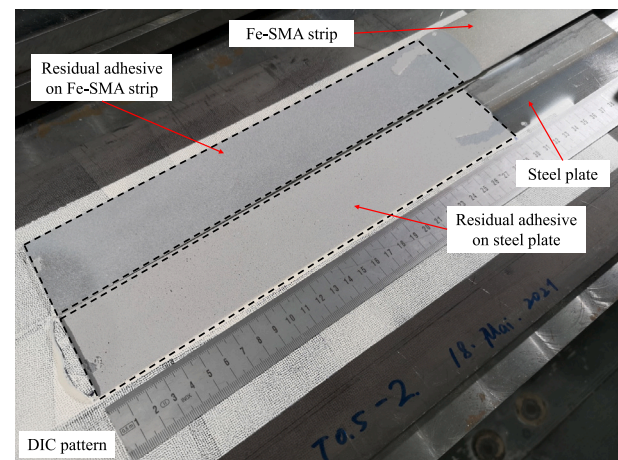
In the beginning of the loading process, almost all materials remain elastic, see stage (i) in Fig. 10. Fig. 10(b), where Fe-SMA tensile stress and strain are plotted, indicates that the stress and strain perfectly align when the load level is low (stage (i)). We note that the stress is scaled from the strain by a factor of 180 GPa, which is reported as the elastic modulus of Fe-SMA at low stress level (lower than 80 MPa) by Yang et al. [22].

4.2.2. Damage accumulation stage

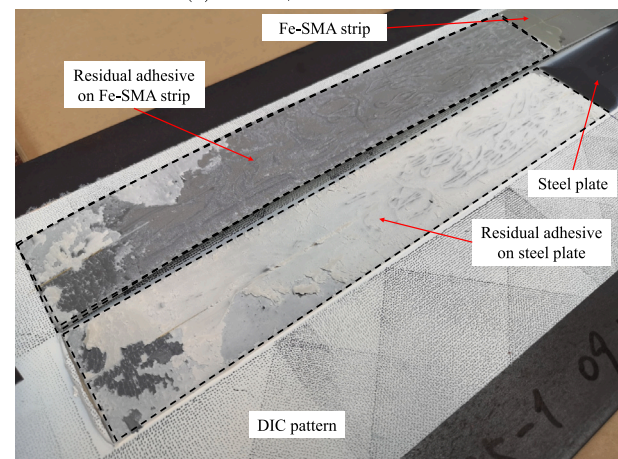
As the force and displacement increase, the stress and strain within the Fe-SMA increase, while shear stress at the loaded end decreases after reaching a peak point, as is evident in stage (ii) of Fig. 10(d), which implies that damage has occurred at the loaded end. In this stage, the stress-strain relationship of the Fe-SMA is no longer linear. Fig. 10(b) shows that when the stress level is lower than 120 MPa, stress and strain exhibit a linear relationship; when exceeding this boundary, the tensile strain develops faster than the tensile stress. This implies that the linearity of the Fe-SMA applies up to ca. 120 MPa. The exhibited nonlinearity beyond this point is attributed to the plasticity and phase transformation [22].

4.2.3. Debonding propagation stage

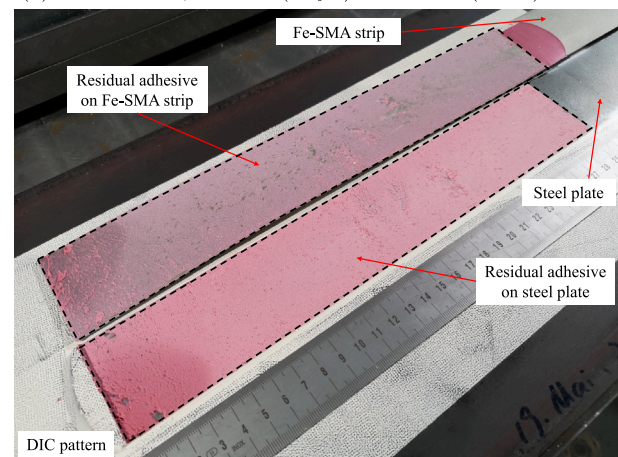
When the force-displacement relationship enters a plateau, the loaded end is fully damaged (shear stress becomes zero) and debonding starts. During the propagation of debonding, stages (iii) - (v) in Fig. 10, the tensile force, maximum tensile strain, maximum tensile stress, and maximum shear stress do not further increase but fluctuate around a threshold; the strain gradient, tensile stress gradient, and shear stress profile move toward the free end (left side in the figures), while maintaining their shapes. It is clearly seen that the tensile stress gradient and shear stress profile only reside within a specific length, rather than the entire bond length. This specific length is known as the effective bond length, over which the tensile stress of the Fe-SMA strip is transferred to the steel substrate via shear stress in the adhesive layer [27]. The effective bond lengths for each specimen are listed in Table 2.



(a) Sika 30, cohesion failure.



(b) Araldite 2015, cohesion (major) + adhesion (minor) failure.



(c) Sika 1277, cohesion failure.

Fig. 9. Typical failure modes of three adhesives. In the visual inspection of the residual adhesive on the adherents, the adhesion failure is recognized, if the surface of the adherents (Fe-SMA or steel) is visible; the residue of the adhesive, on the other hand, is treated as the cohesion failure.

4.3. Load-displacement

Fig. 11 illustrates the load-displacement curves of two specimens processed by the two methods, with the force variable reflected in the black curves being measured by the load cell, while the force in the red

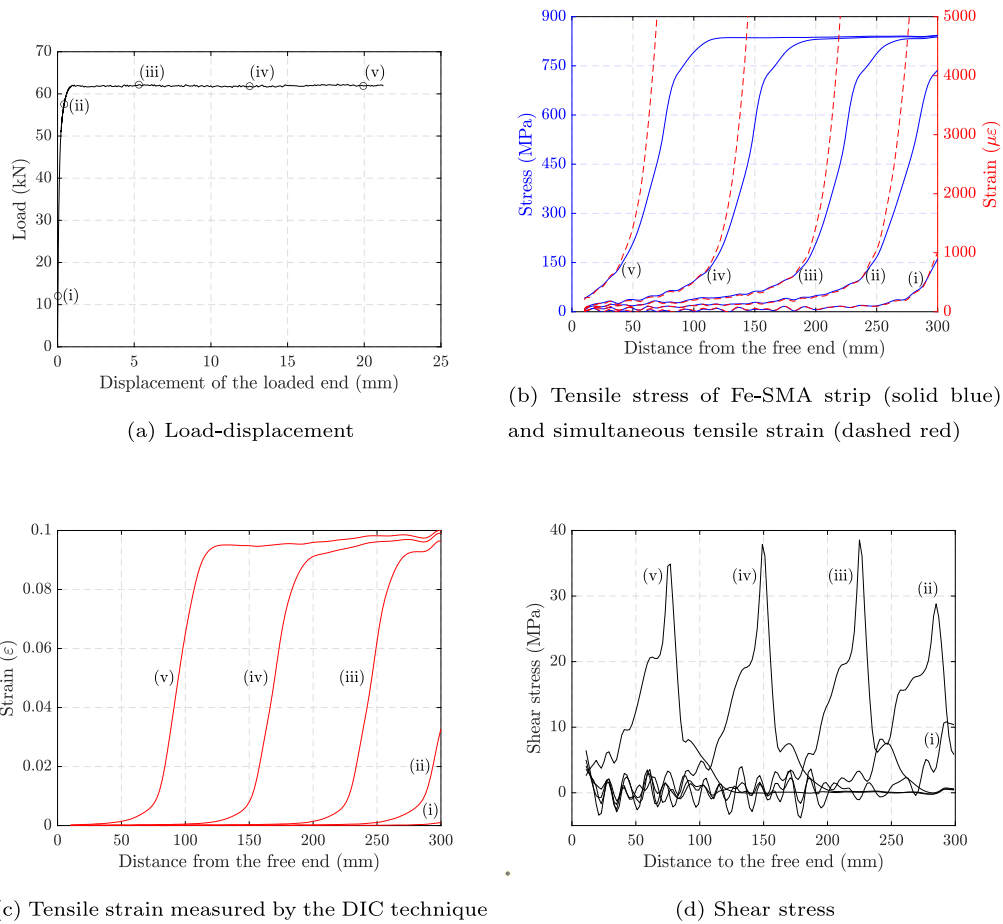


Fig. 10. The full-range mechanical behavior of specimen PS-S2-T0.5-2 with the development of force, displacement, tensile stress, tensile strain, and shear stress at different stages. Stage (i) remains mostly elastic; stage (ii) exhibits obvious nonlinear behavior in the $\sigma - \epsilon$ behavior of Fe-SMA, damage is accumulating in the adhesive; stages (iii)–(v) represent debonding propagation.

curves computed from strain and stress (as described in Section 3.3). Since the Fe-SMA material has high strain rate dependency, the loading speed would affect the mechanical behavior. Fig. 11, however, demonstrates a good match between the measured and processed forces, despite a slight local deviation. This means that the measured stress-strain behavior of the Fe-SMA by means of the dog-bone tensile tests with the designed loading speed represents well that of the Fe-SMA strips in the lap-shear tests, suggesting a good design of the two tests. Such a method of testing Fe-SMA can be used for obtaining material properties when designing bonded strengthening using Fe-SMA strips.

Figs. 12(a)–12(c) summarize the load–displacement behavior of the 24 specimens with force measured by the load cell, sorted in accordance with the adhesives used in the bonded joints. It is observed that the bond capacity of specimens with linear adhesive, i.e., Sika 30, is approximately 35%–45% lower than those with nonlinear adhesives, i.e., Araldite 2015 and Sika 1277. In each joint series, the shear capacity is influenced by the adhesive thickness and the type of Fe-SMA strip (prestrained or not).

In the Sika 30 series, joints with non-prestrained Fe-SMA experience slightly higher bond capacity than those with prestrained Fe-SMA. The reasons are: (i) the tensile stress in the Fe-SMA strips are not high enough to trigger an obvious nonlinear behavior of the Fe-SMA material, which means that the Fe-SMA can be regarded as a linear elastic material; (ii) the non-prestrained Fe-SMA comprises a slightly higher E-modulus than the prestrained one, as shown in Table 1; according to the well-known Eq. (3), a higher E-modulus leads to a higher bond capacity.

$$F_b = b \cdot \sqrt{2 \cdot t \cdot E \cdot G_f} \quad (3)$$

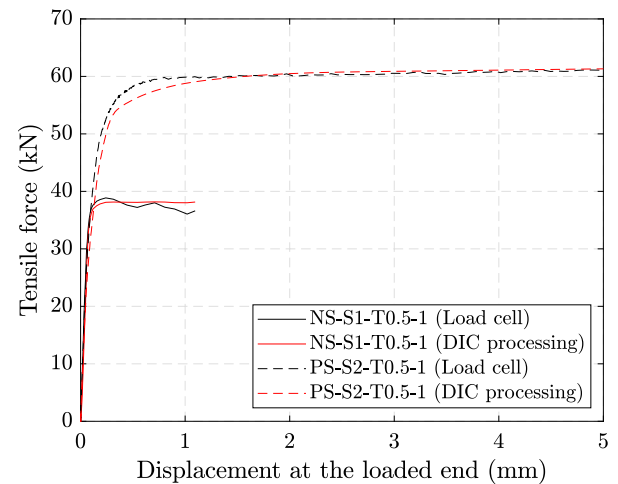


Fig. 11. Load–displacement curves processed from two different methods. Displacement is measured by the DIC technique. Force in black is measured by the load cell, while that in red is computed by multiplying the DIC inferred stress and the cross-sectional area of the Fe-SMA strip. Only displacement up to 5 mm is displayed. (For interpretation of the references to color in this figure legend, the reader is referred to the web version of this article.)

where F_b denotes the bond capacity; t and E are the thickness and E-modulus of the Fe-SMA strip, respectively; b is the bond width (usually

the same as the strip width); G_f represents the interfacial fracture energy of the adhesive bond.

In the two series with nonlinear adhesives, the joints with prestrained Fe-SMA exhibit slightly higher capacity. This is due to the fact that for nonlinear adhesives, the energy needed to break the bond is high, accompanied by high tensile stress level in the Fe-SMA strips, and the nonlinear behavior of the Fe-SMA is triggered. Underneath the non-prestrained and prestrained Fe-SMA strips, adhesives of the same type and thickness comprise similar deformation capacities, resulting in comparable tensile strains in the Fe-SMA strips. As revealed by the stress–strain behavior of the two Fe-SMAs, the prestrained Fe-SMA consistently experiences higher stresses at strain levels similar to the non-prestrained case, within the nonlinear branch. In a parallel study, an analytical model is developed, which has the ability to quantitatively explain the varying bond capacities between different bonded joints. This model describes the bond capacity as a function of (i) the fracture energy of the bond line and (ii) the stress–strain behavior of the adherent. Interested readers are referred to Li et al. [43].

Inside each series with only prestrained Fe-SMA strips, the adhesive thickness also plays a role. The joints with 1 mm adhesive thickness resist higher shear load than those with 0.5 mm adhesive thickness. However, adhesive thickness of 1 mm and 2 mm do not result in obvious difference. This will be further discussed in Section 5.2.

Besides, each of the load–displacement curves in joints with nonlinear adhesives has a long plateau, indicating good ductility of the bonded joint. This is beneficial to the bonded strengthening, since the strengthening system would fail in a late stage (or even later than the failure of the parent structure).

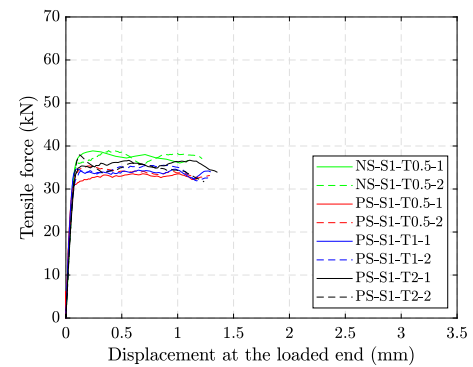
4.4. Bond–slip behavior

Correlating the processed shear stress and measured slip yields the bond–slip behavior, as described in Section 3.4. Two methods of processing the bond–slip behavior are: (i) fixing the location in the bond line and correlating the shear and slip over time; (ii) fixing a time moment and correlating the shear and slip along the bond line. The former one is employed in this study, since it reflects the heterogeneity of the shear behavior along the bond line, which will be discussed in Section 5.4.

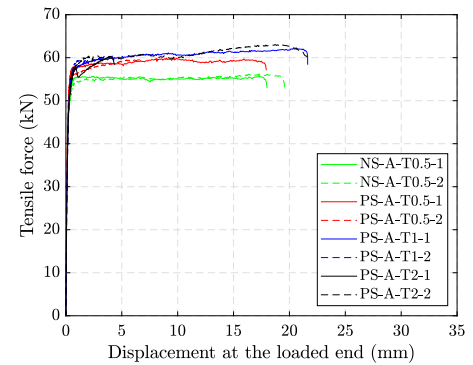
Two types of bond–slip behavior were observed, namely triangular and trilinear bond–slip, see Fig. 13. Joints with linear adhesive have a bond–slip shape with (i) an ascending branch and (ii) a descending branch, which can be simplified as a triangular bond–slip behavior. The bond–slip of joints with nonlinear adhesives comprises three stages: (i) an ascending branch, (ii) a sharp descending branch followed by (iii) a gradual descending branch, which can be simplified to a trilinear behavior. This difference in shape will be discussed in Sections 5.5 and 5.6. The influence of adherent type on the bond–slip curves is not significant. These processed bond–slip curves can be used as input when modeling the bonded joints and the bonded strengthening system using Fe-SMA strips.

5. Further discussion

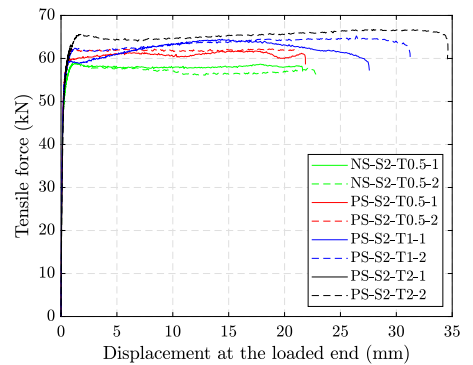
The designed test matrix, as listed in Table 2, aims at investigating the influence of three factors, namely the adhesive type, adhesive thickness, and adherent type, on the bond behavior. The adherent type, namely non-prestrained or prestrained Fe-SMA, was discussed in Section 4.3. The other two factors are to be discussed in what follows.



(a) Load-displacement curves: SikaDur 30 series.



(b) Load-displacement curves: Araldite 2015 series.

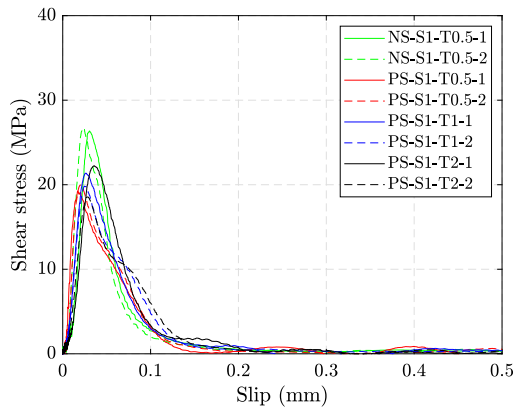


(c) Load-displacement curves: SikaPower 1277 series.

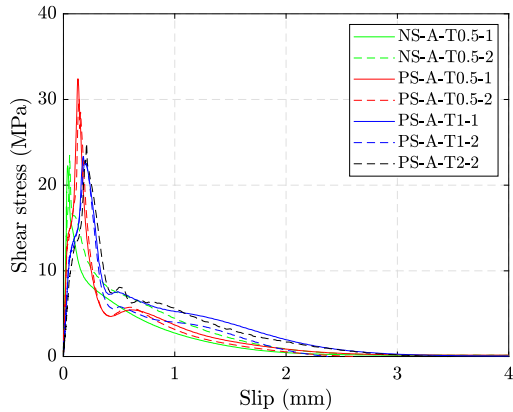
Fig. 12. Load-displacement curves.

5.1. Effect of adhesive type

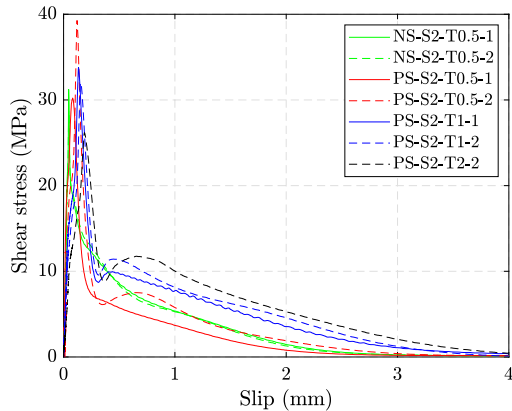
Nonlinear adhesives (Araldite 2015 and Sika 1277), with a larger measured elongation at break, have a higher strain energy (area covered by the stress–strain curve) compared with the linear adhesive (Sika 30), see Fig. 5. The fracture energy in shear, i.e., the area under the bond–slip curve, is highly positively correlated with the strain energy [44,45]. This implies that, locally, more energy is needed to create new surfaces in the bond line of lap-shear joints with nonlinear adhesives, as evidenced in Fig. 14(a). Globally, it corresponds to higher levels of force and displacement for pulling the lap-shear joint with a nonlinear adhesive, which reflects a higher bond capacity, as illustrated in Fig. 14(b).



(a) SikaDur 30 series, with maximum slips being 0.1 – 0.2 mm.



(b) Araldite 2015 series, with maximum slips being 2 – 3 mm.



(c) SikaPower 1277 series, with maximum slips being 2 – 4 mm.

Fig. 13. Bond-slip curves.

In the meantime, nonlinear adhesives are accompanied by longer effective bond lengths, compared against linear adhesives, as plotted in Fig. 14(c). Such a phenomenon was also observed in adhesively bonded CFRP-to-steel lap-shear joints [46]. A longer effective bond length facilitates a higher transfer of tensile load via shear stress. This is a further contribution of the nonlinear adhesive to a high bond capacity.

Since the Fe-SMA strips experience nonlinear behavior, the well known model estimating the bond capacity (Eq. (3)) is not valid. A proper model predicting the bond capacity of lap-shear joints comprising nonlinear adhesives and nonlinear adherents, namely linking Figs. 14(a) and 14(b), is of much importance.

5.2. Effect of adhesive thickness

In addition, adhesive thickness further affects the mechanical behavior of the bonded joints. Fig. 14(a) illustrates, for the same adhesive, the fracture energy of the bond line with a thickness of ca. 1 mm is larger than that with a thickness of ca. 0.5 mm. However, the fracture energy does not significantly differ between adhesive thicknesses of 1 mm and 2 mm. Fig. 14(b) reflects that, for the same adhesive type, the bond capacity of a joint with an adhesive thickness of ca. 1 mm is larger than the capacity corresponding to a thickness of ca. 0.5 mm. For a further increase of the adhesive thickness to ca. 2 mm, the bond capacity of a joint with linear adhesive enhances slightly, while those with nonlinear adhesives remain almost constant.

This implies that thicker adhesives comprise a higher fracture energy, leading to higher bond capacities, however, with a certain cap. This is due to the fact that when the adhesive layer is thin, the plastic zone and fracture process zone are confined by the adherents, namely the Fe-SMA strip and steel plate, with limited energy to dissipate. When the adhesive layer becomes thicker, the size of the plastic zone and fracture process zone expand, with increased fracture energy. However, when the size saturates, there should be a limit for the fracture energy, which in reality comprises the plastic energy and the fracture energy. An extreme case would be a lap-shear joint with a sufficiently thick adhesive layer; only the top layer of adhesive (close to the Fe-SMA strip) is loaded and damaged, similar to concrete members with an externally bonded reinforcement (EBR) with CFRP strips [47–49].

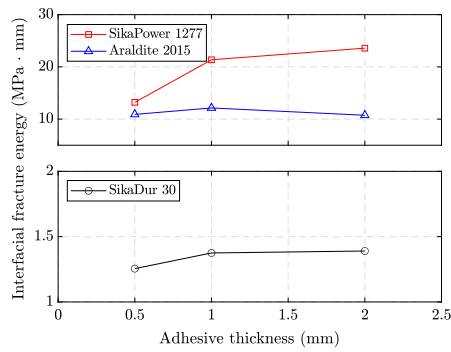
Within the range of tested adhesive thickness, the effective bond length increases with an increase in adhesive thickness, as illustrated in Fig. 14(c). The reason may again be related to the increased plastic and fracture process zones, which expand not only over the thickness direction but also toward the longitudinal direction, leading to increased effective bond length. However, in this case, a limit (cap) should exist as well.

Moreover, it is noted that the stiffness of the bonded joints decreases with an increasing adhesive thickness, as is evidenced in Fig. 14(d). This is due to the fact that the stiffness is computed in the ascending branch in the $F-\Delta$ curve, where the adhesive behaves elastoplastically. Assuming that, in the thickness direction, every point of the adhesive shares the same shear strain (including elastic and plastic strains), the accumulated shear deformation of a thicker adhesive is larger, reflecting a decreased stiffness. It should be noted that in engineering applications, the bonded joints are preferred to behave without damage or with minimal damage, which corresponds to the ascending branch in the $F-\Delta$ behavior. Therefore, the stiffness of bonded joints is of salient importance, which merits further study in the future.

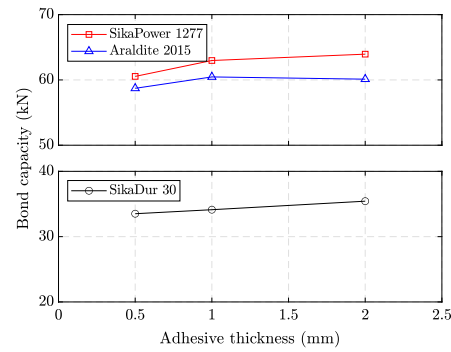
In summary, within the range of the tested adhesive thickness (0.5 to 2 mm), it is demonstrated that an increase in adhesive thickness enhances the load transferring capacity of bonded joints, while reducing the joint stiffness. For the design of bonded strengthening systems, engineers could select the adhesive thickness based on whether a high load transferring capacity or joint stiffness is desirable. In addition, a proper thickness of the adhesive layer, which offers both sufficiently high bond capacity and joint stiffness, could be chosen.

5.3. Is a full-cohesion failure important?

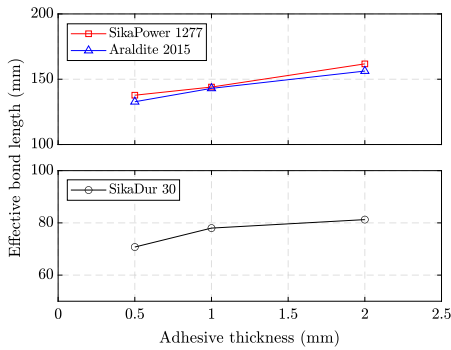
In the previous section Section 4.1, it was reported that the Sika 1277 adhesive experienced full cohesion failure, while the Araldite 2015 encountered minor adhesion failure. However, both yield similarly high bond capacities, which led to five joints with prestrained



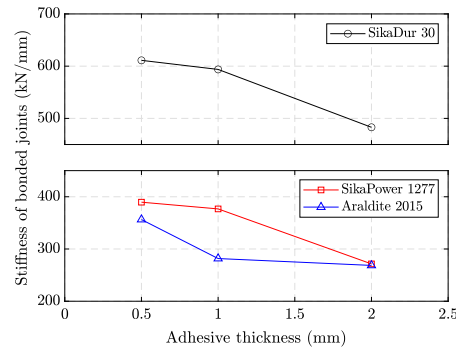
(a) The fracture energy. The upper figure depicts behavior for nonlinear adhesives and corresponds to higher interfacial fracture energy.



(b) The bond capacity. The upper figure depicts behavior for nonlinear adhesives and corresponds to higher bond capacity.



(c) The effective bond length. The upper figure depicts behavior for nonlinear adhesives and corresponds to longer effective bond length.



(d) The joint stiffness. The upper figure depicts behavior for linear adhesive and corresponds to higher joint stiffness.

Fig. 14. Effect of adhesive type and adhesive thickness with the adherent comprising a prestrained Fe-SMA strip. The values of fracture energy, bond capacity, effective bond length, and joint stiffness are computed as an average of the two nominally identical specimens.

Fe-SMA strips failing with Fe-SMA rupture. The repeatability of tested joints which present minor adhesion failure is good in terms of bond capacity and load–displacement results. This means that despite the minor adhesion failure, the mechanical behavior of joints with Araldite 2015 adhesive is reliable, with stable bond–slip curves and high bond capacities in a mild laboratory environment.

However, along the long-term service of steel structures strengthened by bonded Fe-SMA strips, the adhesive–adherent interface is subject to water/salt penetration, similar to the bonded strengthening with CFRP in an harsh environment [50,51]. Bonded joints comprising Fe-SMA strips with higher proportion of adhesion failure in the mild environment are more likely to be corroded in the interface in a salty environment, leading to significantly reduced bond capacity [52]. Proper surface treatment, such as painting primer, can mitigate the adhesion failure and enhance the protection against corrosion [52]. However, such studies on surface treatment for Fe-SMA are very limited.

5.4. Variability of the fracture energy along the bond line

As mentioned in Section 4.4, the bond–slip behavior is processed by fixing the position while correlating shear stress with slip over time. This enables the access to the local bond behavior along the bond line, which can be divided into three regions: (i) the loaded end of the bond, (ii) the middle section, and (iii) the free end, see Fig. 15. In the middle section (region (ii)), the fracture energy is fluctuating around a threshold, which indicates heterogeneity of the bond behavior with respect to the distance from the free end. The reasons could be

the uneven adhesive thickness, the inclusion of pores in the adhesive layer, and the error introduced by the DIC measurement. At the loaded end (region (i)), the processed fracture energy is unstable, and its mechanical behavior is different from that in region (ii), as the artificial debonding tip is straight (see Section 2.2), rather than curved as in the propagation process (see Section 5.7), and the artificial debonding tip is not as sharp as a natural debonding tip, which requires more energy to drive the debonding initiation. When the debonding develops to the free end, region (iii), the remaining bond length (less than the effective bond length) is not enough to hold the tensile load, leading to a sudden debonding failure. No gradual fracture behavior is captured by the DIC cameras in this case. Therefore, in region (iii), the processed fracture energy (not the real fracture energy) is low or even zero. Thus, the bond–slip behavior and the fracture energy in region (ii) are retained as characteristic traits of the bond behavior across the entire bond line.

The authors normalized the fracture energy of each specimen at different locations in region (ii) using Eq. (4).

$$G_{f(i,j,norm)} = \frac{G_{f(i,j)} - \mu_i G_f}{\sigma_i G_f} \quad (4)$$

where $G_{f(i,j,norm)}$ refers to the normalized fracture energy of specimen- i at position- j in region (ii); $G_{f(i,j)}$ means the originally processed fracture energy of specimen- i at position- j in region (ii); $\mu_i G_f$ and $\sigma_i G_f$ represent the mean value and the standard deviation of the originally processed fracture energy of specimen- i at all locations in region (ii).

In total, 3390 normalized fracture energy values from all 24 specimens are collected. A probability density function (PDF) of the normalized fracture energy values, which well approximates a standard

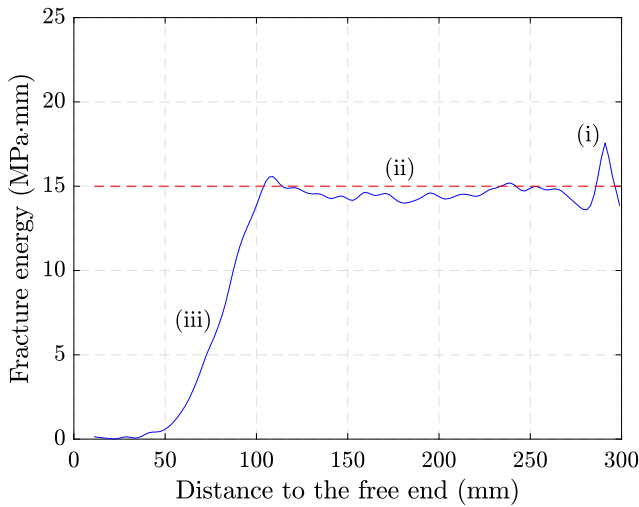


Fig. 15. The processed fracture energy along the bond line over three regions: (i) the loaded end of the bond, (ii) the middle section, and (iii) the free end. Specimen PS-S2-T0.5-2 is employed as an example.

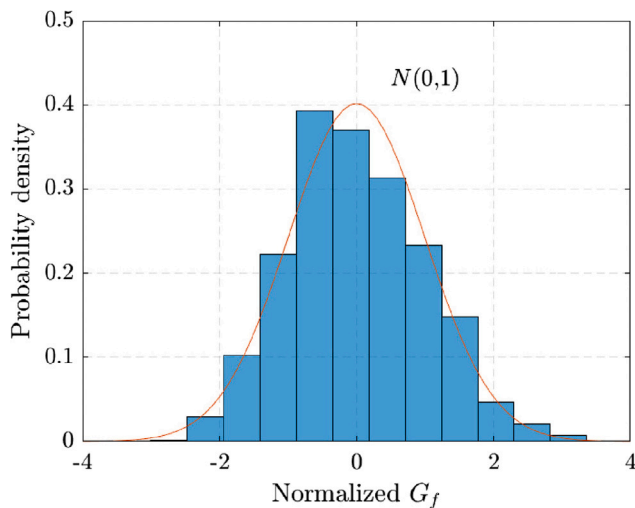


Fig. 16. Histogram and Gaussian Probability Density Function approximation of the normalized interfacial fracture energy of all 24 specimens.

Gaussian distribution, is summarized, as illustrated in Fig. 16. It enables the future stochastic analysis of the mechanical behavior of Fe-SMA-to-steel lap-shear joints. The mean value of the fracture energy can be easily obtained from region (ii) in a lap-shear test; the standard deviation is suggested to be evaluated by the multiplication of the mean value of G_f of the measurement with a coefficient of variance (CoV) of 0.23, which is the mean CoV estimated by the 24 specimens. Interestingly, the maximum and minimum normalized fracture energy are approximately ± 3 , suggesting a standard Gaussian distribution with two bounds of ± 3 , which corresponds to a probability of 99.7%.

5.5. Comparison with the CFRP-to-steel bonded joints

The CFRP-to-steel lap-shear joints have been investigated for almost two decades. We here offer a comparison against this well studied alternative in order to gain a better understanding of the function of Fe-SMA-to-steel lap-shear joints. Two CFRP-to-steel single-lap shear joints (tested by the authors [46]) with the same geometry and adhesives are selected for comparison. The CFRP strips have a thickness of 1.4 mm (1.5 mm for Fe-SMA strips) and an E-modulus of 156 GPa, which is

very similar to that of the non-prestrained Fe-SMA (153.3 GPa). The linear adhesive is Sika 30 while the nonlinear adhesive is Sika 1277, with the adhesive thickness being kept as ca. 0.5 mm.

Fig. 17 shows a comparison of the mechanical behavior between CFRP and Fe-SMA bonded joints in terms of force–displacement behavior and bond–slip behavior. The mechanical behavior of CFRP bonded joints was measured and post-processed via a procedure that is identical to that employed for Fe-SMA joints. To ensure an equivalent loading speed at the bonded joints, the specimens with CFRP strips were tested at a lower loading speed of 0.003 mm/s at the hydraulic actuator, while that for the specimens with Fe-SMA strips was 0.02 mm/s. It is clearly seen in Figs. 17(a) and 17(b) that the joints with the linear adhesive have very similar mechanical behaviors, regardless of adherent being CFRP or Fe-SMA. The reason is that only the quasi-linear stage of the Fe-SMA is used (the maximum tensile stress is ca. 460 MPa) and the chord E-modulus is 153.3 GPa, which is very close to the E-modulus of 156 GPa of the CFRP strip. This implies that when linear adhesive is used in bonding, the two types of bonded joints with CFRP and Fe-SMA strips behave very similarly.

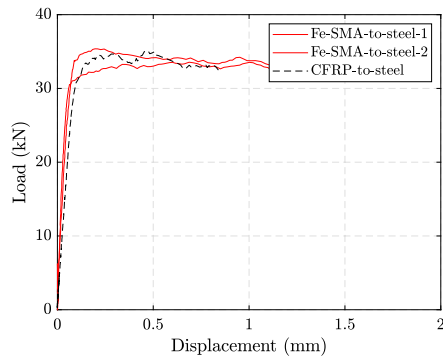
Figs. 17(c) and 17(d) show apparent differences between a CFRP bond and an Fe-SMA bond with a nonlinear adhesive. The Fe-SMA-to-steel bonded joint possesses a bond capacity of 59 kN, while that of CFRP-to-steel bonded joint is 120 kN, approximately 100% larger. Their bond–slip curves follow the same ascending branch until ca. 20 MPa. After this point, the Fe-SMA curve increases up to ca. 33 MPa and then suddenly drops to ca. 15 MPa with a small slip, followed by a gradual decrease to zero shear stress with a maximum slip of ca. 3 mm. The CFRP bond features instead a trapezoidal bond–slip shape, with a plateau after the ascending stage; the descending curve is rapid with a maximum slip of ca. 0.8 mm. The different bond capacities are attributed to the diverse effective bond lengths, which are ca. 123 mm and 185 mm for the Fe-SMA bond and CFRP bond, respectively. A longer effective bond length enables more shear stress transferring through the bond line, which reflects a higher bond capacity. The reason for the different bond–slip behaviors lies in the difference between the non-linear behavior of the Fe-SMA and the linear elastic behavior of the CFRP. A more detailed quantitative explanation requires thorough modeling, which exceeds the scope of the current experimental study.

The Fe-SMA strip with nonlinear adhesive possesses less bond capacity than the CFRP joint bonded by the same adhesive, as shown in Fig. 17(c). However, its ductility is improved. This would allow the bonded Fe-SMA strengthening not to fail completely under a large deformation of the strengthened steel structures, and a certain level of prestress may be preserved in the system.

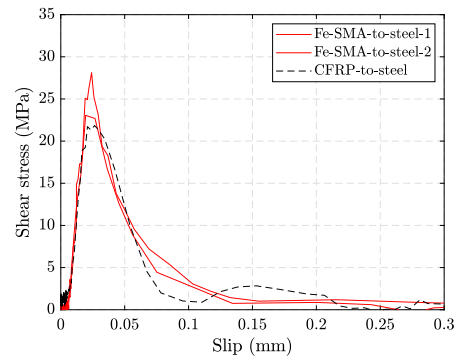
5.6. Shape of the bond–slip curves

A trilinear bond–slip behavior is processed from every Fe-SMA-to-steel lap-shear joint with nonlinear adhesive. Such a trilinear bond–slip was also reported by Schranz et al. [53] and El-Tahan et al. [54], where pull-out tests were conducted on Fe-SMA rebars embedded in concrete blocks and Nickel–Titanium-SMA wires embedded in CFRP composites, respectively. In these studies, friction and mechanical interlock are believed to form the third branch of the bond–slip behavior. However, it is hard to anticipate that friction and mechanical interlock play an important role in the current study, since Fe-SMA strips are free to out-of-plane movement. Fig. 18(a) demonstrates one of the five specimens with Fe-SMA rupture, i.e., PS-A-T1-2, with debonding at the loaded end. After peeling of the Fe-SMA strip, Fig. 18(b) unveils the adhesive fracture surface with three different regions: (i) no damage, (ii) partially damaged, and (iii) fully damaged. Fig. 18(c) depicts the bond–slip behavior processed at different locations (in blue) and the equivalent bond–slip from a CFRP-to-steel joint with the same geometry and adhesive type at the same slip level (in red) [46].

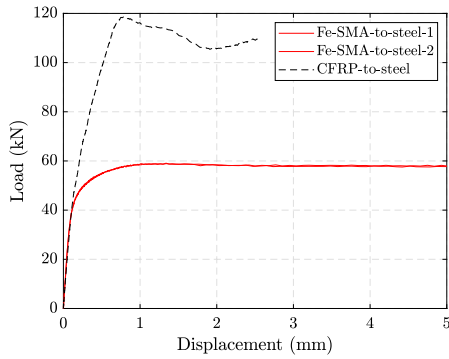
In region (i), no damage due to shear load is visible and the bond–slip behavior is represented by that shown at the location of



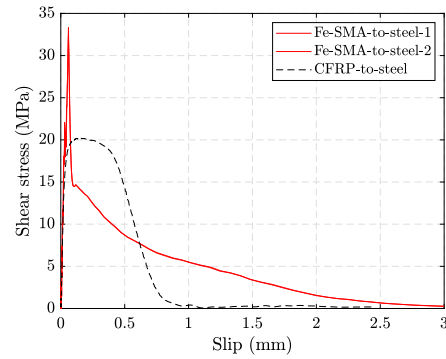
(a) Force-displacement with linear adhesive.



(b) Bond-slip with linear adhesive.



(c) Force-displacement with nonlinear adhesive.



(d) Bond-slip with nonlinear adhesive.

Fig. 17. Bond behavior comparison between Fe-SMA-to-steel bonded joints and CFRP-to-steel bonded joints. The red solid curves are from the Fe-SMA bond, while the black dashed curves are from the CFRP bond. In these joints, the adhesive thickness is ca. 0.5 mm; Fe-SMA strips are non-prestrained; the linear adhesive is Sika 30; the nonlinear adhesive is Sika 1277. (For interpretation of the references to color in this figure legend, the reader is referred to the web version of this article.)

$x = 238$ mm, the ascending branch with elastoplastic behavior of the adhesive; the bond-slip behaviors in both the Fe-SMA bond and CFRP bond are similar. In region (ii), some local damage at the location of $x = 244$ mm can be observed close to the edge of the width direction; the bond-slip processed from the experiment (in blue) drops significantly, while the equivalent bond-slip in the CFRP bond only drops slightly. At the end of region (ii), i.e., location of $x = 254$ mm, a full damage (debonding) is about to occur, evidenced in the fracture surface, and the equivalent bond-slip from the CFRP bond drops almost to zero shear stress, which is reasonable; however, the bond-slip processed from the Fe-SMA bond is non-zero, which seems not true based on the visual inspection on the fracture surface. In region (iii), the processed bond-slip of the Fe-SMA bond just drops to zero shear stress at the location of $x = 276$ mm, which should have already debonded in an earlier stage.

This suggests that the processed trilinear bond-slip with a very long tail cannot well match the observed formation of debonding in the fracture surface. Meanwhile, this observation can be better described by an equivalent trapezoidal bond-slip from a CFRP bonded joint. Justification of this observation requires detailed modeling, which forms part of a future study.

5.7. The curved shape of the Fe-SMA strain gradient

As displayed earlier in Fig. 7, the 2D strain contours of the Fe-SMA strip are not straight but curved. Fig. 19 further focuses on the strain contour and adhesive fracture surface around the debonding tip. The curved strain contour is a result of the 2-dimensional stress/strain behavior of the Fe-SMA strip. The adhesive underneath confines the lateral deformation of the Fe-SMA strip, generating a tensile stress in

the width direction in the Fe-SMA strip (high in the middle and zero at the edge). Eq. (5), when ignoring the shear stress, describes the Von Mises stress in the Fe-SMA strip; the Von Mises stress σ_v is lower than the longitudinal tensile stress component σ_x in the middle of the width direction. This means the plastic flow is hindered there by the lateral stress σ_y , and the total strain, which is measured by the DIC technique, is lower than that at the edge. As a result, at the location where debonding is not fully developed, the strain in the middle of the Fe-SMA strip is lower than that at the edge, see Fig. 19(b). When debonding happens, on the other hand, the strain contour flips the direction: the strain in the middle section results higher than at the edge. Detailed 2D modeling is needed to explain this flipping phenomenon.

$$\sigma_v = \sqrt{\sigma_x^2 - \sigma_x \cdot \sigma_y + \sigma_y^2} \quad (5)$$

where σ_x and σ_y refer to as the tensile stress in the longitudinal direction resulted from the external load and transverse stress due to lateral confinement from the adhesive, respectively; σ_v denotes the Von Mises stress.

The curved strain contour (Fig. 19(b)) can further explain the curved debonding tip (Fig. 19(a)). In Fig. 19(a), a black dashed curve is plotted to distinguish the non-debonding zone from the debonding zone. The debonding zone, where new surfaces in the bond line gradually formed under shear load, developed during the lap-shear test before the rupture of the Fe-SMA strip; the non-debonding zone, where the bond remained intact during the lap-shear test, was unveiled after peeling of the Fe-SMA strip. By shifting the black dashed curve in Fig. 19(a) to the same location in Fig. 19(b), the strain contours on the Fe-SMA strip corresponding to the non-debonding and debonding zones can be easily distinguished. A lower strain corresponds to a smaller

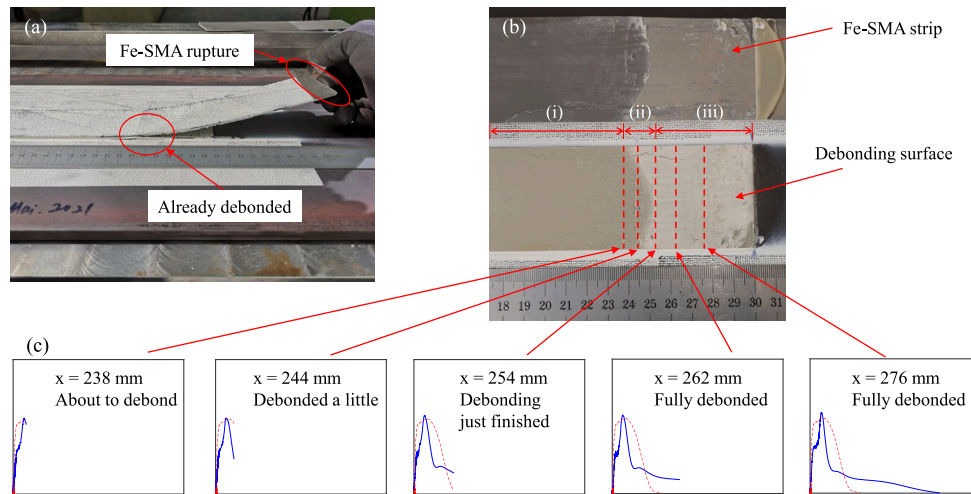


Fig. 18. Bond-slip behavior developed at different positions (x refers to the distance to the free end), with specimen PS-A-T1-2 as an example. (a) Partial debonding when the Fe-SMA strip ruptured; (b) fracture surface after the Fe-SMA peeled from the specimen with three regions: (i) no damage, (ii) partially damaged, and (iii) fully damaged; (c) bond-slip curves, with the blue curves derived from the Fe-SMA bond and the red being computed from the CFRP bond. (For interpretation of the references to color in this figure legend, the reader is referred to the web version of this article.)

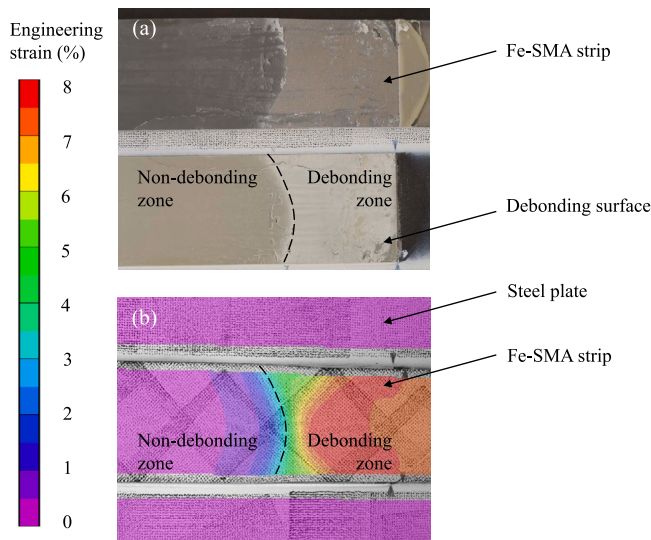


Fig. 19. Specimen PS-A-T1-2 (the same specimen as shown in Fig. 18) failed with debonding at the loaded end and Fe-SMA rupture: (a) the debonding surface after peeling the Fe-SMA strip and (b) the strain contour short before debonding, with purple color, green color, and red color reflecting low, intermediate, and high strain levels, respectively. Figures (a) and (b) are formed synchronously. The black dashed curve denotes the boundary between the non-debonding and debonding zones. (For interpretation of the references to color in this figure legend, the reader is referred to the web version of this article.)

longitudinal deformation of the Fe-SMA strip, which leads to smaller shear deformation in the adhesive underneath. As a result, damage of the adhesive layer in the middle develops slower compared with that at the edge, as shown in Fig. 19(a). In the non-debonding zone, the adhesive behaves within the elastoplastic range; no visible damage occurs or only limited damage accumulates close to the boundary. The tensile strain and stress on the boundary are ca. 1.1% and 645 MPa, respectively. In the debonding zone, the tensile strain and stress accumulate to ca. 8% and 815 MPa, respectively. This means the damage in the adhesive layer accumulate until the full debonding.

The curved strain contour (Fig. 19(b)) and curved debonding tip (Fig. 19(a)) point out that debonding does not happen simultaneously in the width direction, which corresponds to different instantaneous

bond-slip behaviors. This means the processed 1D behavior, which is degenerated from the 2D behavior, as explained in Section 3, is an average behavior in the width direction, rather than an accurate local behavior. In the meantime, some errors might have been introduced in the analysis.

6. Conclusion

In this experimental study, 24 single-lap shear tests of Fe-SMA-to-steel adhesively bonded joints, which comprise two types of adherents, three types of adhesives, and three adhesive thicknesses, were conducted. The mechanical behavior was analyzed and compared with that of CFRP-to-steel joints with the same geometry and adhesive type. The following conclusions can be drawn:

1. The mechanical behavior of Fe-SMA-to-steel bonded joints can be divided into three stages: (i) the elastic stage, where tensile stress in Fe-SMA strips is less than 120 MPa, (ii) the damage accumulation stage, and (iii) the debonding propagation stage, where shear stress profile does not change its shape but shifts toward the free end.
2. The influence of the adherent type (Fe-SMA prestrained or not) on the bond behavior depends on whether the nonlinearity of adherent is triggered. If the adherent remains in its quasi-linear stage, a higher adherent E-modulus offers a larger bond capacity; if the adherent enters the nonlinear stage, the adherent with higher stress behavior is accompanied by higher bond capacity.
3. In Fe-SMA bonded joints, the linear adhesive (Sika 30) has a triangular bond-slip shape, while nonlinear adhesives (Araldite 2015 and Sika 1277) have a trilinear bond-slip shape.
4. The adhesive type and adhesive thickness affect the bond behavior via the fracture energy. A more ductile adhesive or a thicker adhesive layer has larger energy to be dissipated, leading to a greater bond capacity; this is accompanied by a longer effective bond length. The enhanced bond capacity and effective bond length should, however, be limited. The stiffness of bonded joints, on the other hand, decreases with the increasing adhesive thickness.
5. When linear adhesive (Sika 30) is used for bonding, the Fe-SMA bond and CFRP bond have almost identical load-displacement behaviors and triangular bond-slip curves. Significant difference in the bond behavior exists if nonlinear adhesive (Sika 1277)

is used; the bond capacity of the CFRP joint, which has a trapezoidal bond–slip behavior, is twice as that of the Fe-SMA joint, which has a trilinear bond–slip behavior.

CRedit authorship contribution statement

Lingzhen Li: Investigation, Formal analysis, Methodology, Writing – original draft. **Wandong Wang:** Formal analysis, Methodology, Supervision, Writing – review & editing. **Eleni Chatzi:** Supervision, Writing – review & editing. **Elyas Ghafoori:** Conceptualization, Supervision, Writing – review & editing.

Declaration of competing interest

The authors declare that they have no known competing financial interests or personal relationships that could have appeared to influence the work reported in this paper.

Data availability

Data will be made available on request.

Acknowledgments

The first author would like to acknowledge the China Scholarship Council (CSC) for co-financing his PhD study. Sika AG and Huntsman GmbH are acknowledged to provide adhesives. The authors acknowledge the support from re-fer AG, Switzerland, in providing the Fe-SMA materials for this study. Thanks also go to the technical assistance from Empa technicians, Mr. Giovanni Saragoni, Mr. Slavko Tudor, and Mr. Robert Widmann.

Appendix. Strain computation and its types

In this study, all the data processing are on the basis of strain measurement using the DIC technique and the stress–strain behavior measured by Fe-SMA dog-bond samples. Hence, it is worthy to understand how the strain is computed with the DIC technique, which is very similar to the strain computation in the finite element (FE) analysis. The black speckled pattern on the white background, described in Section 2.2, are captured by the stereo camera system. Then, the captured speckles are treated as nodes, and meshes are generated in the analyzing software (Vic-3D). When the specimen is loaded, the black speckles move, which corresponds to the displacement of nodes. The strain can be easily computed via deformation gradient. Note here, the engineering strain, though frequently used in the analysis, is not directly computed, since error would be introduced by rigid body rotation. To avoid such an error, the Lagrangian strain is computed as the default strain in the Vic-3D software and then converted to the engineering strain for later processing. It should also be noted that several types of strain definitions exist, such as Lagrangian strain, engineering strain, and logarithmic strain (i.e., true strain). Their difference at low strain level, e.g., CFRP below 1.5%, can be ignored. However, at high strain level, e.g., some of the Fe-SMA strips in the current study were loaded to 10% strain, a difference of 1% absolute strain would occur among these types of strain. Therefore, when processing stress–strain with large deformation, the type of stress–strain should be clear. Otherwise, errors would be introduced. Interested readers are referred to Vic-3D Software Manual [55] for more details regarding DIC measurement and data processing. The strain definition and computation can be easily found in the literature.

References

- [1] E. Ghafoori, Editorial for special issue on sustainable metallic structures, *Eng Struct* 183 (2019) 83.
- [2] P.C. Chang, A. Flatau, S.-C. Liu, Health monitoring of civil infrastructure, *Struct. Health Monit.* 2 (3) (2003) 257–267.
- [3] I. Olofsson, L. Elfgren, Sustainable bridges: Assessment for future traffic demands and longer lives, in: *International Conference on Bridge Maintenance, Safety and Management*: 18/10/2004-22/10/2004, Taylor and Francis Group, 2004, pp. 369–370.
- [4] R. Haghighi, M. Al-Emrani, M. Heshmati, Fatigue-prone details in steel bridges, *Buildings* 2 (4) (2012) 456–476.
- [5] X. Ye, Y. Su, J. Han, A state-of-the-art review on fatigue life assessment of steel bridges, *Math. Probl. Eng.* 2014 (2014).
- [6] X. Shao, J. Cao, Fatigue assessment of steel-UHPC lightweight composite deck based on multiscale FE analysis: Case study, *J. Bridge Eng.* 23 (1) (2018) 05017015.
- [7] H. Martín-Sanz, K. Tatsis, D. Damjanovic, I. Stipanovic, A. Sajna, I. Duvnjak, U. Bohinc, E. Brühwiler, E. Chatzi, Getting more out of existing structures: steel bridge strengthening via UHPFRC, *Front. Built Environ.* 5 (2019) 26.
- [8] Q.-Q. Yu, X.-L. Zhao, R. Al-Mahaidi, Z.-G. Xiao, T. Chen, X.-L. Gu, Tests on cracked steel plates with different damage levels strengthened by CFRP laminates, *Int. J. Struct. Stab. Dyn.* 14 (06) (2014) 1450018.
- [9] T. Chen, L. Li, N. Zhang, X. Song, Y. Hidekuma, Fatigue performance test on inclined central cracked steel plates repaired with CFRP strand sheets, *Thin-Walled Struct.* 130 (2018) 414–423.
- [10] T. Ummenhofer, P. Weidner, Improvement factors for the design of welded joints subjected to high frequency mechanical impact treatment, *Steel Constr.* 6 (3) (2013) 191–199.
- [11] K. Yamada, T. Ishikawa, T. Kakiuchi, et al., Rehabilitation and improvement of fatigue life of welded joints by ICR treatment, *Adv. Steel Construct.* 11 (3) (2015) 294–304.
- [12] A. Hosseini, E. Ghafoori, M. Motavalli, A. Nussbaumer, X.-L. Zhao, Mode I fatigue crack arrest in tensile steel members using prestressed CFRP plates, *Compos. Struct.* 178 (2017) 119–134.
- [13] H. Heydarinouri, A. Nussbaumer, M. Motavalli, E. Ghafoori, Strengthening of steel connections in a 92-year-old railway bridge using prestressed CFRP rods: Multiaxial fatigue design criterion, *J. Bridge Eng.* 26 (6) (2021) 04021023.
- [14] T. Chen, X.-L. Gu, M. Qi, Q.-Q. Yu, Experimental study on fatigue behavior of cracked rectangular hollow-section steel beams repaired with prestressed CFRP plates, *J. Compos. Construct.* 22 (5) (2018) 04018034.
- [15] B. Zheng, M. Dawood, Fatigue strengthening of metallic structures with a thermally activated shape memory alloy fiber-reinforced polymer patch, *J. Compos. Construct.* 21 (4) (2017) 04016113.
- [16] L. Li, T. Chen, X. Gu, E. Ghafoori, Heat activated SMA-CFRP composites for fatigue strengthening of cracked steel plates, *J. Compos. Construct.* 24 (6) (2020) 04020060.
- [17] A.I. Abdy, M.J. Hashemi, R. Al-Mahaidi, Fatigue life improvement of steel structures using self-prestressing CFRP/SMA hybrid composite patches, *Eng. Struct.* 174 (2018) 358–372.
- [18] G. Yuan, Y. Bai, Z. Jia, K.-t. Lau, P.-y. Hung, Structural deformation performance of glass fiber reinforced polymer composite beam actuated by embedded indented SMA wires, *Composites B* 159 (2019) 284–291.
- [19] M. Tazarv, M. Saïd Saïdi, Reinforcing NiTi superelastic SMA for concrete structures, *J. Struct. Eng.* 141 (8) (2015) 04014197.
- [20] X.-L. Gu, Z.-Y. Chen, Q.-Q. Yu, E. Ghafoori, Stress recovery behavior of an Fe-Mn-Si shape memory alloy, *Eng. Struct.* 243 (2021) 112710.
- [21] M. Shahverdi, J. Michels, C. Zaderski, M. Motavalli, Iron-based shape memory alloy strips for strengthening RC members: Material behavior and characterization, *Constr. Build. Mater.* 173 (2018) 586–599.
- [22] Y. Yang, M. Breveglieri, M. Shahverdi, Effect of phase changes on the axial modulus of an FeMnSi-shape memory alloy, *Materials* 14 (17) (2021) <http://dx.doi.org/10.3390/ma14174815>.
- [23] M. Izadi, E. Ghafoori, M. Motavalli, S. Maalek, Iron-based shape memory alloy for the fatigue strengthening of cracked steel plates: Effects of re-activations and loading frequencies, *Eng. Struct.* 176 (2018) 953–967.
- [24] M. Izadi, A. Hosseini, J. Michels, M. Motavalli, E. Ghafoori, Thermally activated iron-based shape memory alloy for strengthening metallic girders, *Thin-Walled Struct.* 141 (2019) 389–401.
- [25] J. Vůjtek, P. Ryjáček, J.C. Matos, E. Ghafoori, Iron-based shape memory alloy for strengthening of 113-year bridge, *Eng. Struct.* 248 (2021) 113231.
- [26] W. Wang, L. Li, A. Hosseini, E. Ghafoori, Novel fatigue strengthening solution for metallic structures using adhesively bonded Fe-SMA strips: A proof of concept study, *Int. J. Fatigue* 148 (2021) 106237.
- [27] W. Wang, A. Hosseini, E. Ghafoori, Experimental study on Fe-SMA-to-steel adhesively bonded interfaces using DIC, *Eng. Fract. Mech.* 244 (2021) 107553.
- [28] M. Izadi, E. Ghafoori, M. Shahverdi, M. Motavalli, S. Maalek, Development of an iron-based shape memory alloy (Fe-SMA) strengthening system for steel plates, *Eng. Struct.* 174 (2018) 433–446, <http://dx.doi.org/10.1016/j.engstruct.2018.07.073>.

- [29] A. Cladera, B. Weber, C. Leinenbach, C. Czaderski, M. Shahverdi, M. Motavalli, Iron-based shape memory alloys for civil engineering structures: An overview, *Constr. Build. Mater.* 63 (2014) 281–293.
- [30] H. Zhou, D. Fernando, J.L. Torero, J.P. Torres, C. Maluk, R. Emberley, Bond behavior of CFRP-to-steel bonded joints at mild temperatures: experimental study, *J. Compos. Construct.* 24 (6) (2020) 04020070.
- [31] M. Banea, L.d. Silva, R. Campilho, Effect of temperature on tensile strength and mode I fracture toughness of a high temperature epoxy adhesive, *J. Adhes. Sci. Technol.* 26 (7) (2012) 939–953.
- [32] A. Al-Shawaf, R. Al-Mahaidi, X.-L. Zhao, Effect of elevated temperature on bond behaviour of high modulus CFRP/steel double-strap joints, *Aust. J. Struct. Eng.* 10 (1) (2009) 63–74.
- [33] W. Khalil, L. Saint-Sulpice, S.A. Chirani, C. Bouby, A. Mikolajczak, T.B. Zineb, Experimental analysis of Fe-based shape memory alloy behavior under thermomechanical cyclic loading, *Mech. Mater.* 63 (2013) 1–11.
- [34] M. Mohri, I. Ferretto, C. Leinenbach, D. Kim, D.G. Lignos, E. Ghafoori, Effect of thermomechanical treatment and microstructure on pseudo-elastic behavior of Fe–Mn–Si–Cr–Ni–(V, C) shape memory alloy, *Mater. Sci. Eng. A* (2022) 143917.
- [35] C. Leinenbach, W. Lee, A. Lis, A. Arabi-Hashemi, C. Cayron, B. Weber, Creep and stress relaxation of a FeMnSi-based shape memory alloy at low temperatures, *Mater. Sci. Eng. A* 677 (2016) 106–115, <http://dx.doi.org/10.1016/j.msea.2016.09.042>.
- [36] E. Hosseini, E. Ghafoori, C. Leinenbach, M. Motavalli, S.R. Holdsworth, Stress recovery and cyclic behaviour of an Fe–Mn–Si shape memory alloy after multiple thermal activation, *Smart Mater. Struct.* 27 (2) (2018) 025009, <http://dx.doi.org/10.1088/1361-665x/aaa2c9>.
- [37] ISO 527-2:2012. Plastics – determination of tensile properties – Part 2: Test conditions for moulding and extrusion plastics, 2012.
- [38] J. Michels, J. Sena Cruz, R. Christen, C. Czaderski, M. Motavalli, Mechanical performance of cold-curing epoxy adhesives after different mixing and curing procedures, *Composites B* 98 (2016) 434–443, <http://dx.doi.org/10.1016/j.compositesb.2016.05.054>.
- [39] D. Fernando, J.-G. Teng, T. Yu, X.-L. Zhao, Preparation and characterization of steel surfaces for adhesive bonding, *J. Compos. Construct.* 17 (6) (2013) 04013012.
- [40] F. Niccoli, M. Alfano, L. Bruno, F. Furguele, C. Maletta, Mechanical and functional properties of nickel titanium adhesively bonded joints, *J. Mater. Eng. Perform.* 23 (7) (2014) 2385–2390.
- [41] J.-G. Teng, D. Fernando, T. Yu, X. Zhao, Treatment of steel surfaces for effective adhesive bonding, in: *Advances in FRP Composites in Civil Engineering*, Springer, 2011, pp. 865–868.
- [42] A. Kwakernaak, J. Hofstede, J. Poulis, R. Benedictus, Improvements in bonding metals (steel, aluminium), in: *Advances in Structural Adhesive Bonding*, Elsevier, 2010, pp. 185–236, <http://dx.doi.org/10.1533/9781845698058.2.185>.
- [43] L. Li, C. Eleni, E. Ghafoori, Debonding model for nonlinear Fe-SMA strips bonded with nonlinear adhesives, *Eng. Fract. Mech.* (2022) (submitted for publication).
- [44] S.H. Xia, J.G. Teng, Behavior of FRP-to-steel bonded joints, in: *Proceedings of the International Symposium on Bond Behaviour of FRP in Structures, BBFS 2005*.
- [45] D. Fernando, T. Yu, J.G. Teng, Behavior of CFRP laminates bonded to a steel substrate using a ductile adhesive, *J. Compos. Construct.* 18 (2) (2014) 04013040, [http://dx.doi.org/10.1061/\(ASCE\)CC.1943-5614.0000439](http://dx.doi.org/10.1061/(ASCE)CC.1943-5614.0000439).
- [46] L. Li, N. Pichler, E. Chatzi, E. Ghafoori, Estimation of the mechanical behavior of CFRP-to-steel bonded joints with quantification of uncertainty, *Eng. Struct.* 266 (2022) 114573.
- [47] J. Michels, E. Zile, C. Czaderski, M. Motavalli, Debonding failure mechanisms in prestressed CFRP/epoxy/concrete connections, *Eng. Fract. Mech.* 132 (2014) 16–37.
- [48] P. Colombi, G. Fava, C. Poggi, End debonding of CFRP wraps and strips for the strengthening of concrete structures, *Compos. Struct.* 111 (2014) 510–521.
- [49] C. Czaderski, K. Soudki, M. Motavalli, Front and side view image correlation measurements on FRP to concrete pull-off bond tests, *J. Compos. Construct.* 14 (4) (2010) 451.
- [50] M. Dawood, S. Rizkalla, Environmental durability of a CFRP system for strengthening steel structures, *Constr. Build. Mater.* 24 (9) (2010) 1682–1689.
- [51] M. Heshmati, R. Haghani, M. Al-Emrani, Durability of bonded FRP-to-steel joints: Effects of moisture, de-icing salt solution, temperature and FRP type, *Composites B* 119 (2017) 153–167.
- [52] N. Pichler, W. Wang, J.A. Poulis, E. Ghafoori, Surface preparations and durability of iron-based shape memory alloy adhesively bonded joints, *Int. J. Adhesion Adhesives* (2022) (submitted for publication).
- [53] B. Schranz, C. Czaderski, T. Vogel, M. Shahverdi, Bond investigations of prestressed, near-surface-mounted, ribbed memory-steel bars with full bond length, *Mater. Des.* 196 (2020) 109145.
- [54] M. El-Tahan, M. Dawood, Bond behavior of NiTiNb SMA wires embedded in CFRP composites, *Polym. Compos.* 39 (10) (2018) 3780–3791.
- [55] Correlated Solution, Vic-3D Software Manual, URL <http://www.correlatedsolutions.com/supportcontent/VIC-3D-8-Manual.pdf>.